



ELSEVIER

Dynamics of Atmospheres and Oceans 21 (1995) 227–256

dynamics
of atmospheres
and oceans

Regimes and scaling laws for rotating deep convection in the ocean

Barry A. Klinger^{*}, John Marshall

Center for Meteorology and Physical Oceanography, Department of Earth, Atmospheric, and Planetary Sciences, Massachusetts Institute of Technology, Cambridge MA 02139, USA

Received 4 November 1993; revised 29 April 1994; accepted 28 June 1994

Abstract

Numerical experiments are presented which explore the dependence of the scale and intensity of convective elements in a rotating fluid on variations in external parameters in a regime relevant to open ocean deep convection. Conditions inside a convection region are idealized by removing buoyancy at a uniform rate B from the surface of an initially homogeneous, motionless, incompressible ocean of depth H with a linear equation of state, at a latitude where the Coriolis parameter is f . The key nondimensional parameters are the natural Rossby number $Ro^* = (B/f^3 H^2)^{1/2}$ and the flux Rayleigh number $Ra_f = BH^4/(\kappa^2 \nu)$, where κ and ν are (eddy) diffusivities of heat and momentum. Ro^* is set to values appropriate to open ocean deep convection ($0.01 < Ro^* < 1$), and moderately high values of Ra_f ($10^4 < Ra_f < 10^{13}$) were chosen to produce flows in which nonlinear effects are significant. The experiments are in the ‘geostrophic turbulence’ regime.

As Ro^* and Ra_f are reduced the convective elements become increasingly quasi-two-dimensional and can be described as a field of interacting ‘hetons’. The behavior of the flow statistics—plume horizontal length scale L , speed scale U and buoyancy scale G , and the magnitude of the mean adverse density gradient measured by the stratification parameter H —are studied as a function of Ro^* and Ra_f . Physically motivated scaling laws are introduced, which, when appropriate, employ geostrophic and hydrostatic constraints. They are used to interpret the experiments. In the heton regime, in which the motion is predominantly geostrophic and hydrostatic, the observed scales are sensitive to moderate variations in Ro^* and large variations in Ra_f . We demonstrate broad agreement between our numerical experiments and previous laboratory studies. The lateral scale of the convective elements and the (adverse) stratification in which they exist adjust to one another so that $NH/fL \approx 1$; the horizontal scale of the hetons is thus controlled by a pseudo Rossby radius based on the unstable stratification parameter N , the scale at which the overturning

^{*} Corresponding author. Present address: Nova Southeastern University Oceanographic Center, Dania, FL 33004, USA.

forces associated with N are balanced by the counter-overturning forces associated with rotation.

1. Introduction

In this paper we present numerical experiments with a non-hydrostatic convection model in which a neutral, rotating ocean is subject to horizontally uniform buoyancy loss at its upper surface. We attempt to understand, and rationalize with physically motivated scaling laws, those processes that control the scales and intensity of the ensuing convection. The study is motivated by the desire to elucidate the character of rotationally modified convection in a parameter regime relevant to open ocean deep convection, an important mode of deep water mass formation and a key component of the global thermohaline circulation of the ocean. Our results have relevance to the ‘convective elements’ or ‘plumes’, regions of upwelling and downwelling of $O(1 \text{ km})$ width that stir newly dense water down to great depth. They are also pertinent to recent laboratory studies of rotating convection by Fernando et al. (1991) (henceforth FCB), Boubnov and Golitsyn (1986, 1990) and Chen et al. (1989).

Our experiments numerically explore convection in a rotating, neutral fluid at high Rayleigh number and low natural Rossby number, with ocean convection specifically in mind. They are analogous to, but carried out in a different parameter regime from, the ‘large eddy’ simulations of the atmospheric boundary layer reported by, for example, Mason (1989). Oceanic convection is in a distinctly different parameter regime from such atmospheric convection. The natural Rossby number $Ro^* = L_{rot}/H$ (Maxworthy and Narimousa, 1991, 1994; Jones and Marshall, 1993), a ratio comparing the vertical scale $L_{rot} = (B/f^3)^{1/2}$ at which convection comes under the influence of the Earth’s rotation, to the depth of the convective layer H , is large in the atmosphere but small in the ocean. Here B is the buoyancy flux extracted at the ocean’s surface and f is the Coriolis parameter. Typical vertical heat fluxes achieved by a population of convective elements in the atmospheric and oceanic boundary layer are comparable. However, the vertical buoyancy flux in the atmosphere exceeds that in the ocean by many orders of magnitude. The ratio of the buoyancy fluxes in the two fluids for a given heat flux is

$$\frac{B_{atmos}}{B_{ocean}} = \frac{\rho_W c_W}{\rho_A \alpha c_A \theta_A} \quad (1)$$

where ρ is the density, c is the specific heat, θ_A is a typical air temperature, and α is the coefficient of thermal expansion of water, and subscripts W and A represent water and air, respectively.

Inserting typical values ($\rho_W = 1000 \text{ kgm}^{-3}$, $\rho_A = 1 \text{ kgm}^{-3}$, $\alpha = 2 \times 10^{-4} \text{ K}^{-1}$, $c_W = 4000 \text{ Jkg}^{-1}\text{K}^{-1}$, $c_A = 1000 \text{ Jkg}^{-1}\text{K}^{-1}$, and $\theta_A = 300 \text{ K}$), we find that atmospheric buoyancy fluxes are 10^5 times greater than oceanic buoyancy fluxes, giving an L_{rot} of 100 km or more in the atmosphere. Typical vertical scales are set by the depth of the troposphere, $H = 10 \text{ km}$, giving $Ro^* \approx 10$; the convection ‘hits the

ceiling' before it feels the effect of rotation. (We are considering here the effect of rotation on the individual convective elements themselves; convective complexes in the atmosphere will be organized, however, on the L_{rot} scale.) In the ocean, by contrast, where the buoyancy forcing is much weaker, $L_{\text{rot}} \approx 500$ m and the depth of deep-reaching convection is $H \approx 2$ km, so that $\text{Ro}^* \approx 0.25$ and rotation cannot be ignored. Oceanic convection, therefore, is in a somewhat unfamiliar, but fascinating parameter regime and is studied here by numerical experiment.

High-resolution experiments are presented to investigate the scales and intensity of the convective elements on the external parameters of the system. Sensitivity of the flow to the natural Rossby number Ro^* and the flux Rayleigh number $\text{Ra}_f = \text{BH}^4 / (\kappa^2 \nu)$ is probed by varying the rotation rate, diffusivity, and total depth of the system. As described in Section 2, Ro^* is an especially useful nondimensional parameter because it measures the importance of rotation in a convecting system and is independent of diffusivity of momentum and heat. We attempt to understand, to the extent that it is possible, the observed flows in terms of variations of Ro^* alone, because we believe that at sufficiently high Rayleigh number, Ro^* becomes the controlling nondimensional parameter. Using molecular values or diffusivity of temperature and momentum in water ($\kappa \approx 10^{-7} \text{ m}^2 \text{ s}^{-1}$, $\nu \approx 10^{-6} \text{ m}^2 \text{ s}^{-1}$), we find that the flux Rayleigh number is approximately 10^{27} , a very large number, indicating that the flow must be highly turbulent. Flows with such high Rayleigh number cannot be simulated with computers available at present ($\text{Ra}_f \approx 10^{13}$ is achieved here) and we must parameterize the turbulent mixing process. We choose to employ Laplacian friction and diffusivity parameterizations (with Austausch coefficients representing the transfer of momentum and heat by subgrid-scale turbulent processes) rather than a more sophisticated turbulence closure scheme. The simplicity and analytical amenability of such an approach makes it attractive. Perhaps more importantly, it allows us to define relevant nondimensional parameters unambiguously and makes possible direct comparisons of our numerical simulations with the laboratory experiments mentioned in the first paragraph.

In this contribution we draw together, and attempt to present in a rational way, the key scaling laws for the convective elements, and the physical assumptions on which they are based. In particular, we exploit, when appropriate, hydrostatic and geostrophic constraints which lead to scaling laws which can be described by simple formulae. We find broad quantitative agreement between our numerical experiments and the afore-mentioned laboratory studies. Use of a numerical model, however, enables us to probe and describe in more detail the physical balances which control the structure and intensity of rotationally controlled convection.

2. Nondimensional parameters

The physical system of interest here is characterized by a small number of external parameters—the total fluid depth H , the imposed surface buoyancy flux

B , the Coriolis parameter f (twice the rotation rate), the kinematic viscosity ν and the diffusivity of buoyancy κ . This system can be completely described by three nondimensional parameters. We highlight the importance of the ‘natural Rossby number’ Ro^* of Maxworthy and Narimousa (1991),

$$Ro^* = \left(\frac{B}{f^3 H^2} \right)^{1/2} \quad (2)$$

which is a measure of the importance of rotation and is independent of the diffusivities. The complementary parameter is the flux Rayleigh number,

$$Ra_f = \frac{BH^4}{\kappa^2 \nu} \quad (3)$$

which is independent of rotation and measures the influence of diffusion of momentum and buoyancy. The third nondimensional parameter is the Prandtl number,

$$Pr = \nu / \kappa \quad (4)$$

a measure of the relative strengths of diffusion of momentum and buoyancy. Here we suppose that $Pr = 1$.

In the classical literature on rotating convection, Ro^* is not employed and the system is described in terms of Ra_f and the Taylor number, which depends on both f and the diffusivity:

$$Ta = \left(\frac{fH^2}{\nu} \right)^2 \quad (5)$$

Here, however, we choose to rationalize our experiments in terms of (Ra_f , Ro^*) because this pairing produces a tidy division of the external parameters between a viscous–diffusive parameter and a rotational parameter. Such a division is especially useful for application to the ocean, where poorly known eddy diffusivities are more relevant to the behavior than molecular diffusivities. Appropriate values of Ra_f and Ta for oceanic deep convection are difficult to determine, but Ro^* is easy to calculate. At the site of deep convection in the western Mediterranean Sea, $H \approx 2000$ m, $f \approx 10^{-4}$ s $^{-1}$, and $B \approx 4 \times 10^{-7}$ m 2 s $^{-3}$ (Leaman and Schott, 1991), which implies $Ro^* = 0.3$. If we take ‘deep’ convection to encompass regimes from Labrador Sea to Weddell Sea deep water formation, then relevant values for H range from about 1000 m to 4000 m, B ranges from perhaps 10^{-7} m 2 s $^{-3}$ to perhaps 5×10^{-7} m 2 s $^{-3}$, and f ranges from its Mediterranean value up to 1.5×10^{-4} s $^{-1}$. Therefore values of Ro^* from about 0.01 to 1 are most relevant to oceanic deep convection.

Boubnov and Golitsyn (1986, 1988, 1990), Boubnov and Ivanov (1988), Chen et al. (1989), Fernando et al. (1989) and FCB conducted experiments in which a rotating tank of water was heated uniformly from below, and aspects of the flow and temperature fields of the resulting convection were measured. Nonrotating experiments were also conducted. Boubnov and Golitsyn (1990) employed a regime

diagram, reproduced by FCB, which divides the Ta – Ra_f plane into regions which are, for increasing flux Rayleigh number and natural Rossby number: the conduction regime, in which diffusion suppresses the convective instability; a regime of regular structure, in which convection takes the form of uniform cells; a geostrophic turbulence regime; a fully turbulent regime. With a flux Rayleigh number Ra_f in the range of 2×10^{12} to 9×10^{12} and Ta of 10^9 to 2×10^{11} , FCB's rotating experiments are in the geostrophic turbulence regime. The natural Rossby number was not employed by FCB or Boubnov and Golitsyn (1986, 1990), but we can deduce from their published parameters that Ro^* ranged from 0.0006 to 0.033 (FCB) and from approximately 10^{-4} to approximately unity (Boubnov and Golitsyn).

Postulating that diffusive effects are negligible in the high flux Rayleigh number regime of their laboratory experiments, FCB deduced from dimensional considerations that, in the nonrotating case, scales for speed (U m s⁻¹), buoyancy (G m s⁻²), and length (L m) are

$$U_{\text{non}} = (BH)^{1/3}, \quad G_{\text{non}} = (B^2/H)^{1/3}, \quad L_{\text{non}} = H \quad (6)$$

and for the rotating case they are

$$U_{\text{rot}} = (B/f)^{1/2}, \quad G_{\text{rot}} = (Bf)^{1/2}, \quad L_{\text{rot}} = (B/f^3) \quad (7)$$

Golitsyn (1980) also derived the same rotating scaling for velocity based on consideration of the dissipation of energy by the convecting system.

The scales in (6) and (7) were discussed at some length by Jones and Marshall (1993). It is useful to note that $U_{\text{rot}}/U_{\text{non}} = Ro^{*1/3}$, $G_{\text{rot}}/G_{\text{non}} = Ro^{*-1/3}$, and $L_{\text{rot}}/L_{\text{non}} = Ro^*$, so that the rotational and nonrotational scales converge at $Ro^* = 1$.

FCB showed that the above scalings for U and G are appropriate for the nonrotating and rotating (low Ro^*) cases. In the rotating case, they also found that these quantities were independent of depth and time, at least at distances greater than $5L_{\text{rot}}$ from the boundary where a heat flux was imposed. The characteristics of the convection studied by FCB correspond to the 'geostrophic turbulence' regime of Boubnov and Golitsyn (1990). The experiments of Boubnov and Golitsyn (1990) also showed that the velocity scale was relatively insensitive to f in the fully turbulent regime.

Similar experiments were carried out at small Ro^* by Maxworthy and Narimousa (1991, 1994) and Brickman and Kelley (1994a,b), and numerically by Jones and Marshall (1993) and by Raasch and Etling (1991). Focusing on the first stage of the flow, Maxworthy and Narimousa (1994) found that velocities scaled with U_{rot} , and Jones and Marshall found velocity and buoyancy consistent with the rotational scaling (7). Raasch and Etling conducted three numerical experiments ($0.005 \leq Ro^* \leq 0.065$) in which a turbulence closure scheme was used to parameterize subgrid-scale processes. They found that the vertical velocity had a dependence on f consistent with the rotational scaling, but the statistics for horizontal speed and buoyancy were much less dependent on f .

There remain a number of unresolved issues, however, which motivate the present study. There is no clear understanding of the observed scales of the convection; Boubnov and Golitsyn (1990) did not find that $L \approx L_{\text{rot}}$, and instead presented an empirical scaling law dependent on the Rayleigh number and Taylor number, but without physical motivation. FCB did not explicitly discuss the observed horizontal scale of the elements that occupy the body of the convecting fluid. In numerical experiments, such as those of Jones and Marshall (1993), the finite and rather coarse resolution of the numerical grid necessitates the use of eddy viscosities and diffusivities, which may play a role in determining the scale of the modeled convection.

3. Experimental procedure and observed regimes

3.1. The numerical experiments

3.1.1. Numerical model description

The incompressible, Boussinesq, Navier–Stokes equations were integrated using a numerical model describing the evolution of a rotating, initially unstratified ocean. The model is a discretization of the following system of equations:

$$\frac{Du}{Dt} + \frac{1}{\rho_0} \frac{\partial \rho'}{\partial x} - fv = \nu_H \left(\frac{\partial^2 u}{\partial x^2} + \frac{\partial^2 u}{\partial y^2} \right) + \nu_V \frac{\partial^2 u}{\partial z^2} \quad (8a)$$

$$\frac{Dv}{Dt} + \frac{1}{\rho_0} \frac{\partial \rho'}{\partial y} + fu = \nu_H \left(\frac{\partial^2 v}{\partial x^2} + \frac{\partial^2 v}{\partial y^2} \right) + \nu_V \frac{\partial^2 v}{\partial z^2} \quad (8b)$$

$$\frac{Dw}{Dt} + \frac{1}{\rho_0} \frac{\partial \rho'}{\partial z} + b = \nu_H \left(\frac{\partial^2 w}{\partial x^2} + \frac{\partial^2 w}{\partial y^2} \right) + \nu_V \frac{\partial^2 w}{\partial z^2} \quad (8c)$$

$$\frac{\partial u}{\partial x} + \frac{\partial v}{\partial y} + \frac{\partial w}{\partial z} = 0 \quad (8d)$$

$$\frac{DT}{Dt} = \kappa_h \left(\frac{\partial^2 T}{\partial x^2} + \frac{\partial^2 T}{\partial y^2} \right) + \kappa_V \frac{\partial^2 T}{\partial z^2} \quad (8e)$$

where (u, v, w) is the velocity in a Cartesian (x, y, z) coordinate system, t is time, ρ_0 is the initial (uniform) density, ρ' is the deviation from the initial hydrostatically balanced pressure field, $b = g\rho'/\rho_0$ is the buoyancy (as in the previous section), T is the temperature, and

$$\frac{D}{Dt} = \frac{\partial}{\partial t} + u \frac{\partial}{\partial x} + v \frac{\partial}{\partial y} + w \frac{\partial}{\partial z} \quad (9)$$

is the substantial derivative. Density was assumed to be a linear function of the temperature:

$$\rho = \rho_0 [1 + \alpha(T - T_0)] \quad (10)$$

Table 1
Standard parameters

Parameter	Symbol	Value
Thermal expansion coefficient	α	$2.1 \times 10^{-4} \text{ } ^\circ\text{C}^{-1}$
Specific heat	c_p	$3900 \text{ J kg}^{-1} \text{ } ^\circ\text{C}^{-1}$
Gravitational constant	g	9.8 m s^{-2}
Reference temperature	T_0	12°C
Reference density	ρ_0	1000 kg m^{-3}
Surface heat flux	Q	$800 \text{ J m}^{-2} \text{ s}^{-1}$

where α is the coefficient of thermal expansion and T_0 is a reference temperature typical of observations during deep convection in the Western Mediterranean (Leaman and Schott, 1991). (See Table 1 for parameters.) The equations were integrated on a staggered grid using the ‘pressure’ method of Harlow and Welch (1965), with a time-differencing scheme consisting of alternate Euler-backward and Euler-forward steps. The domain was periodic in both x and y . The vertical velocity was set to zero at the surface and bottom boundaries, and the vertical heat flux was set to zero at the bottom boundary. The numerical model has been described in more detail by Brugge et al. (1991).

The fluid was cooled by decreasing the temperature in the top level of the domain at each time step at a rate proportional to the surface heat loss. The cooling was uniform on the large scale, but an additional term which varies randomly from gridpoint to gridpoint was added to supply a perturbation to initiate the convective instability. The amplitude of the random term was half the value of the mean cooling.

The numerical experiments were performed in a square domain that was 3200 m on a side, consisting of either 128 gridpoints at intervals of 25 m or 64 gridpoints at intervals of 50 m (see Table 2(a)). Most of the experiments had a vertical grid spacing of 50 m, but coarse vertical resolution was employed in simulations of particularly deep oceans. Details of each run can be found in Table 2(a). Some calculations (see Table 2(b)) were repeated at different spatial resolution to demonstrate that key statistical measures of the ensuing convection did not change when the resolution was changed. Two of the runs in which the plumes were relatively wide were also repeated in larger domains (16 km by 16 km; see Table 2(b), Runs d and e). They showed that the key statistics were insensitive to the size of the domain. In all experiments, a time step of approximately 60 s was employed. A typical high-resolution experiment took about 3 h of CPU time on a Cray Y-MP for 24 h of simulation time.

3.1.2. External and nondimensional parameters

Parameters for the experiments are listed in Table 2. The values of f , H , and B were chosen both to encompass the oceanographically relevant regime and also to elucidate the dynamics of rotationally dominated convection. The natural Rossby number Ro^* ranged from 0.0025 to 0.32, and the horizontal flux Rayleigh number

Table 2(a)
External parameters, numerical experiments

Run	f	$4\pi/f$	H	(κ_H, κ_V)	t_{run}	Ro^*	Ra_f
$\Delta x = 25 \text{ m}, N_x = 128$							
1	1.00	34.9	2	(0.1, 0.1)	96	0.32	6.4×10^9
2	2.52	13.9	2	(0.1, 0.1)	48	0.08	6.4×10^9
3	4.00	8.7	2	(0.1, 0.1)	48	0.04	6.4×10^9
4	10.08	3.5	2	(0.1, 0.1)	72	0.01	6.4×10^9
5	4.00	8.7	1	(0.1, 0.1)	48	0.08	4.0×10^8
6	10.08	3.5	8	(0.1, 0.1)	168	0.0025	1.6×10^{12}
7	4.00	8.7	2	(0.01, 0.01)	48	0.04	6.4×10^{12}
8	4.00	8.7	2	(0.1, 0.1)	48	0.04	6.4×10^6
9	4.00	8.7	2	(1, 0.1)	48	0.04	6.4×10^6
10	10.08	3.5	2	(1, 0.1)	60	0.01	6.4×10^6
11	10.08	3.5	4	(1, 0.1)	84	0.005	1.0×10^8
12	1.00	34.9	2	(5, 0.1)	72	0.32	5.1×10^4
13	4.00	8.7	2	(5, 0.1)	84	0.04	5.1×10^4
14	10.08	3.5	2	(5, 0.1)	180	0.01	5.1×10^4
15	10.08	3.5	1	(5, 0.1)	168	0.02	3.2×10^3
$\Delta x = 50 \text{ m}, N_x = 64$							
16	1.59	22.0	4	(5, 5)	96	0.08	8.2×10^5
17	2.52	13.9	4	(5, 5)	96	0.04	8.2×10^5
18	4.00	8.7	4	(5, 5)	144	0.02	8.2×10^5
19	6.35	5.5	4	(5, 5)	168	0.01	8.2×10^5

f is Coriolis parameter (in units of 10^{-4} s^{-1}), $4\pi/f$ is duration of a pendulum day (h), H is total depth (km), (κ_H, κ_V) are vertical and horizontal components of diffusivity ($\text{m}^2 \text{ s}^{-1}$), t_{run} is duration of run (h), Ro^* is the natural Rossby number, and Ra_f is the flux Rayleigh number, Δx is horizontal grid spacing, N_x is number of gridpoints in each horizontal direction. The vertical grid spacing Δz was 50 m for runs with $H \leq 2$ km, 100 m for $H = 4$ km and 200 m for $H = 8$ km. N_z , the number of levels in the vertical, was 40 for $H \geq 2$ km and 20 for $H = 1$ km. The time step was 30 s for $\Delta x = 25$ m and 60 s for $\Delta x = 50$ m.

ranged from 5×10^4 to 6×10^{12} (see Fig. 1(a)). In all runs, the cooling at the top was $Q = 800 \text{ Wm}^{-2}$, which produced a buoyancy loss of $B = g\alpha Q/\rho c_p = 4 \times 10^{-7} \text{ m}^2 \text{ s}^{-3}$ (c_p , tabulated in Table 2, is the specific heat). For each of our chosen values

Table 2(b)
Parameters, resolution sensitivity tests

Run	f	H	(κ_H, κ_V)	t_{run}	Ro^*	Ra_f	Δx	N_x	d	Δz	N_z
a	1.00	2	(5, 0.1)	48	0.32	5.1×10^4	250	16	4.0	100	20
b	4.00	2	(5, 0.1)	72	0.04	5.1×10^4	250	16	4.0	100	20
c	10.08	2	(5, 0.1)	120	0.01	5.1×10^4	250	16	4.0	100	20
d	1.00	2	(5, 0.1)	48	0.32	5.1×10^4	250	64	16.0	100	20
e	10.08	2	(5, 0.1)	96	0.01	5.1×10^4	250	64	16.0	100	20
f	1.00	2	(0.1, 0.1)	24	0.32	6.4×10^9	50	64	3.2	50	40
g	1.00	2	(0.1, 0.1)	24	0.32	6.4×10^9	50	128	3.2	100	20
h	4.00	2	(0.1, 0.1)	12	0.04	6.4×10^9	25	128	3.2	200	10

Symbols as in Table 2(a). In addition, d is domain width (km).

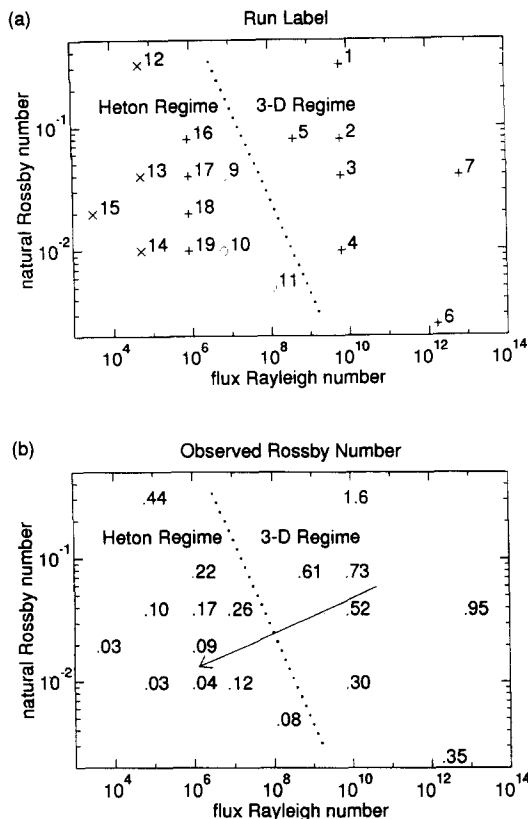


Fig. 1. (a) Run label number (see Table 2) and (b) Rossby number $Ro = U/fL$ (see Section 4) as a function of the flux Rayleigh number Ra_f and natural Rossby number Ro^* for all experiments. Symbol type denotes ratio of horizontal to vertical diffusivity γ : +, $\gamma = 1$; o, $\gamma = 10$; x, $\gamma = 50$. Dotted line shows approximate division between the heton and three-dimensional regimes. Run 8 (not shown) has $\gamma = 1$ and the same Ro^* and Ra_f as Run 9.

of Ra_f , different Ro^* values were obtained by varying f from its terrestrial value of 10^{-4} s^{-1} up to $10 \times 10^{-4} \text{ s}^{-1}$. Ra_f was varied by changing H and κ_H . In all runs, H ranged from 1000 to 8000 m. The diffusivities (κ_H, κ_V) used ranged between 0.01 and $5 \text{ m}^2 \text{ s}^{-1}$ and can be found in Table 2 (see also Fig. 1(a)). Anisotropic diffusivities were used in some experiments to facilitate comparison with the low-resolution results of Jones and Marshall (1993), which had $(\kappa_H, \kappa_V) = (5, 0.1) \text{ m}^2 \text{ s}^{-1}$.

3.2. Observed regimes

Initially, a statically unstable layer of cold water developed at the top of the water column which began to overturn and, ultimately, extended down to the

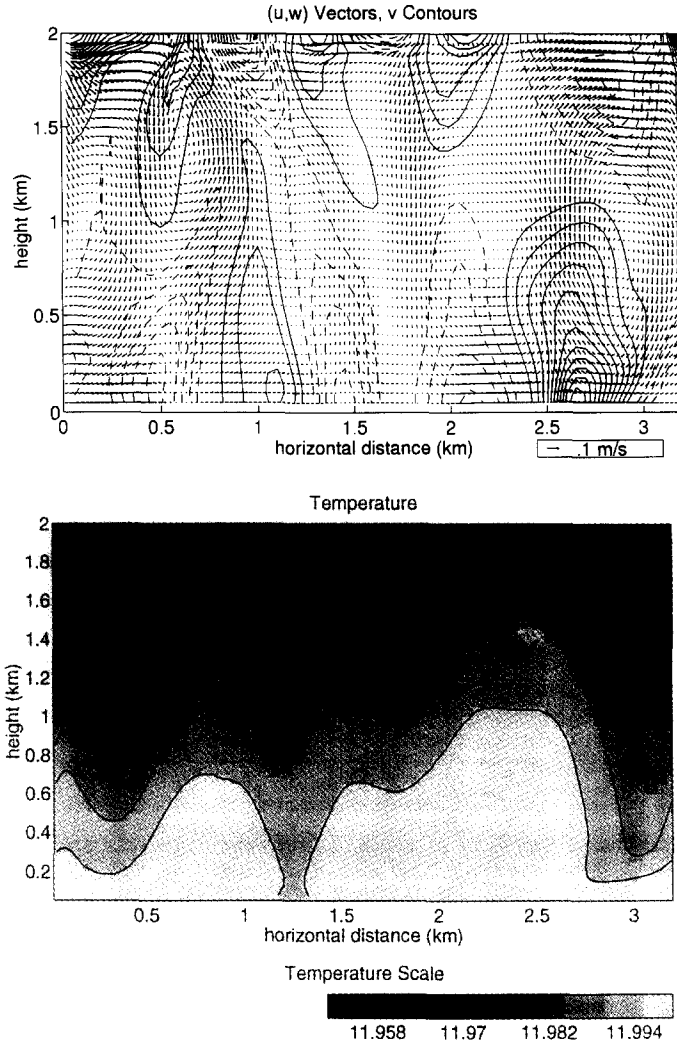


Fig. 2. Typical convective structures in the heton regime, taken from Run 10, with $(Ro^*, Ra_f) = (0.01, 6.4 \times 10^6)$, 48 h after beginning of run. In all plots, the contour interval (c.i.) is equal to one-half the standard deviation of the field unless otherwise noted, with continuous lines indicating contours greater than zero and dashed lines indicating contours less than zero. (a) Velocity in vertical ($x-z$) section, where vectors show components (u, w) in plane and contours show component v perpendicular to plane (c.i. = 0.01 ms^{-1}). (b) Temperature in vertical ($x-z$) section. (c) Horizontal velocity (u, v) and dynamic height h' in horizontal ($x-y$) plane at a depth of 1475 m (c.i. = $2.7 \times 10^{-4} \text{ m}$). (d) Vertical velocity w in horizontal plane at 1475 m depth (c.i. = 0.013 ms^{-1}). (e) Divergence D of horizontal velocity in horizontal plane at a depth of 1475 m (c.i. = $2.1 \times 10^{-5} \text{ s}^{-1}$). (f) Curl ζ of horizontal velocity in horizontal plane at a depth of 1475 m (c.i. = $1.2 \times 10^{-4} \text{ s}^{-1}$).

bottom. Eventually, convection filled the entire water column and a statistically quasi-steady-state was reached. It is this statistically steady state that is the focus of attention here; it was only established after, typically, several rotation periods.

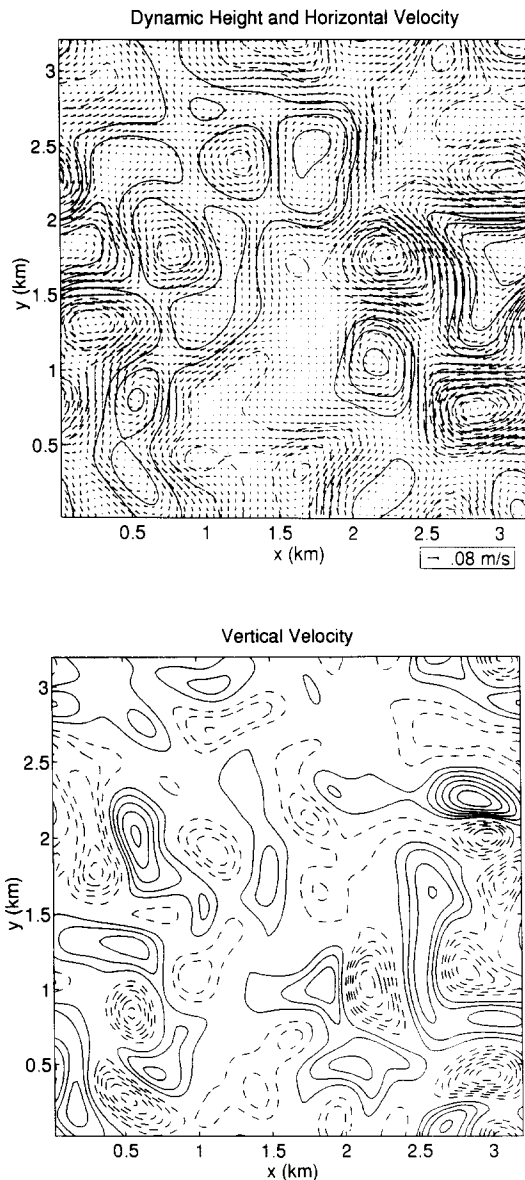


Fig. 2 (continued).

All of our experiments fall within what Bouinov and Golitsyn called the ‘geostrophic turbulence’ regime with $Ro^* < 1$. However, within this regime we observed qualitative and systematic flow differences which can be best characterized in terms of the observed flow Rossby number (see Fig. 1(b)). As Ro^* and Ra_f were reduced the flow comprised distinct ‘heton’ (Hogg and Stommel, 1985; Legg and Marshall, 1993) pairs with counter-rotating flow above and below under

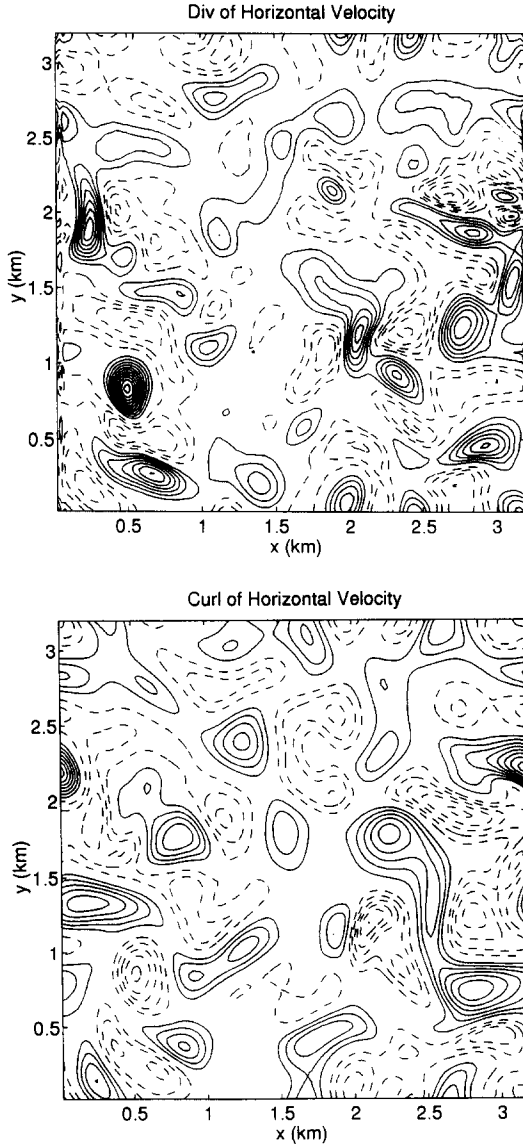


Fig. 2 (continued).

rotational control. As Ro^* and Ra_f were increased we observed convective structures with a richer three-dimensional structure which tended to have a larger Rossby number. The broad transition from the three-dimensional regime to the quasi-two-dimensional heton regime, is indicated by the arrow on the regime diagram (Fig. 1(b)).

Flow fields typical of the heton limit are shown in Fig. 2. Cells can be seen

reaching from the top of the water column to the bottom (Fig. 2(a)). Associated with the sinking or rising currents there are strong horizontally swirling currents. Cyclonic circulation in the top half of the domain tended to be accompanied by anticyclonic circulation directly below and vice versa. A vertical section of temperature (Fig. 2(b)) shows the unstable stratification common to all our experiments, with the isotherms perturbed by the upwelling and downwelling motion. In the heton regime, the isotherm slopes tend to be relatively small and the isotherms undulate gently upward and downward. Similarly, horizontal sections of velocity and dynamic height (Fig. 2(c)), vertical velocity (Fig. 2(d)) and temperature show fields dominated by smooth patterns. The close alignment between isobars and velocity vectors in Fig. 2(c) indicates a high degree of geostrophic control. All runs with $Ro^* < 0.3$ were under geostrophic control.

As shown in Figs. 2(e) and 2(f), there is a rough but striking correspondence between patterns of vertical velocity w and patterns of divergence $D = u_x + v_y$ and relative vorticity $\zeta = v_x - u_y$ (compare Fig. 2(d) with Fig. 2(e)); stretching of the planetary vortex tubes generates cyclonic vorticity, and vice versa (Veronis, 1958). In the heton regime, the upwelling and downwelling regions had similar sizes and strengths.

As shown in Fig. 3(a), vertical sections of velocity in the three-dimensional limit were complicated and exhibited a more complex connection between the various fields than in the heton limit. Vertical velocity w at a given horizontal coordinate changed sign one or more times with depth, whereas (u, v) did not have the simple vertical correlation seen in Fig. 2(a). The temperature field (Fig. 3(b)) displayed structure in the vertical at several different length scales, and the mean isotherm depths were more strongly perturbed than in the heton regime. The fields also had a more complex horizontal structure (Figs. 3(c)–3(f)). Runs in the three-dimensional limit tended to be less geostrophic than runs in the heton limit with similar values of Ro^* , though for $Ro^* \leq 0.01$ the flow was approximately geostrophic (Fig. 3(c)) even in the three-dimensional regime. There was a noticeable asymmetry between upwelling and downwelling regions, with downwelling somewhat more localized and intense, especially towards the surface of the fluid. These surface downwelling structures may correspond to the intense vortices reported by Chen et al. (1989) and FCB.

3.3. Vertical structure as a function of the external parameters

Runs with lower flux Rayleigh number and natural Rossby number tended to have a simpler vertical structure. To quantify this tendency, we calculated vertical empirical orthogonal functions (EOFs) of the vertical velocity field in the final quasi-steady state. This decomposition can be expressed as

$$w(x, y, z) = \sum_i a_i(x, y) C_i(z) \quad (11)$$

where we refer to C_i as the i th mode. In the standard calculation of such empirical orthogonal functions, the modes are ordered in terms of the amount of variance of the function captured by each mode, with the most significant mode coming first.

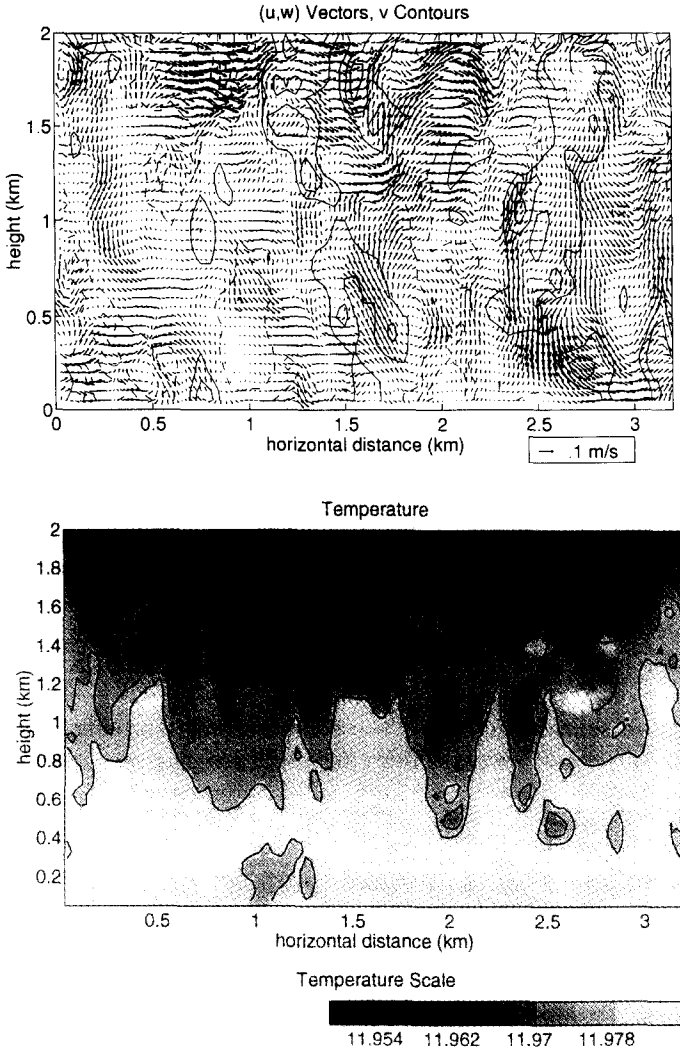


Fig. 3. Typical convective structures in the three-dimensional regime, Run 4, $(Ro^*, Ra_f) = (0.01, 6.4 \times 10^9)$, at 72 h. Contours as in Fig. 2. (a) Velocity in vertical $(x-z)$ section, where vectors show components (u, w) in plane and contours show component v perpendicular to plane (c.i. = standard deviation = 0.026 ms^{-1}). (b) Temperature in vertical $(x-z)$ section. (c) Horizontal velocity (u, v) and dynamic height h' in horizontal $(x-y)$ plane at a depth of 1475 m (c.i. = 3.5×10^{-4} m). (d) Vertical velocity w in horizontal plane at 1475 m depth (c.i. = 0.018 ms^{-1}). (e) Divergence D of horizontal velocity in horizontal plane at a depth of 1475 m (c.i. = $1.0 \times 10^{-4} \text{ s}^{-1}$). (f) Curl ζ of horizontal velocity in horizontal plane at a depth of 1475 m (c.i. = $2.8 \times 10^{-4} \text{ s}^{-1}$). (c)–(f) include only one-quarter of the domain so that the relatively small features can be seen more clearly.

Fig. 4(a) shows the structure of the most significant modes for a typical run. In all runs, the most significant mode was the one with no sign changes in the vertical, with successive modes having one or more sign changes. The percentage of

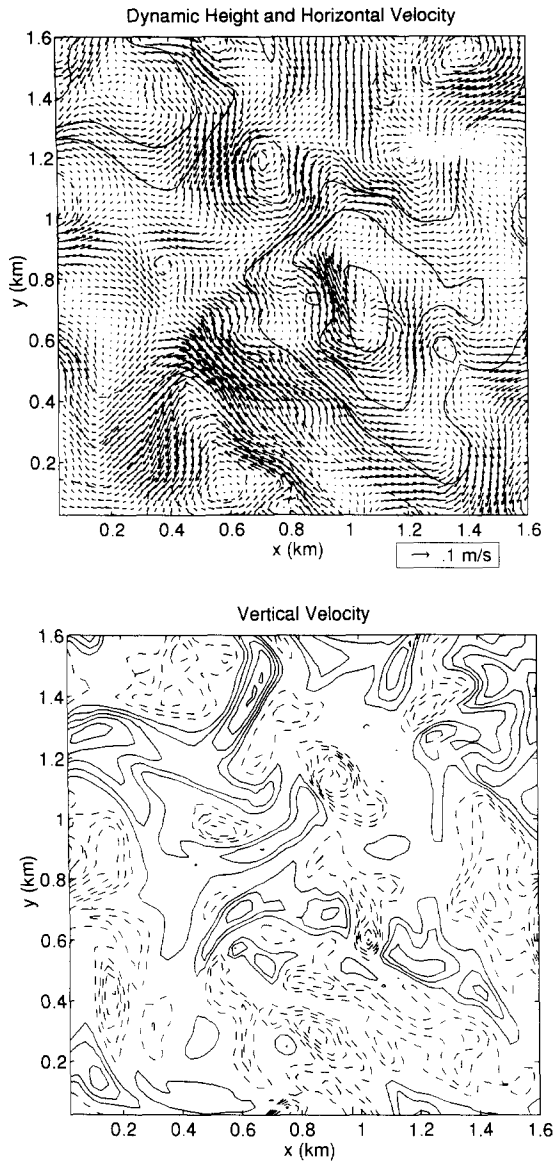


Fig. 3 (continued).

variance in the data accounted for by the first mode is a measure of how two-dimensional the w field was. By examining output from all the experiments, we judged some of the runs to be close to the heton limit and others to be three-dimensional; as Fig. 4(b) shows, runs qualitatively identified as two-dimensional had first-mode strengths which accounted for greater than 60% of the total

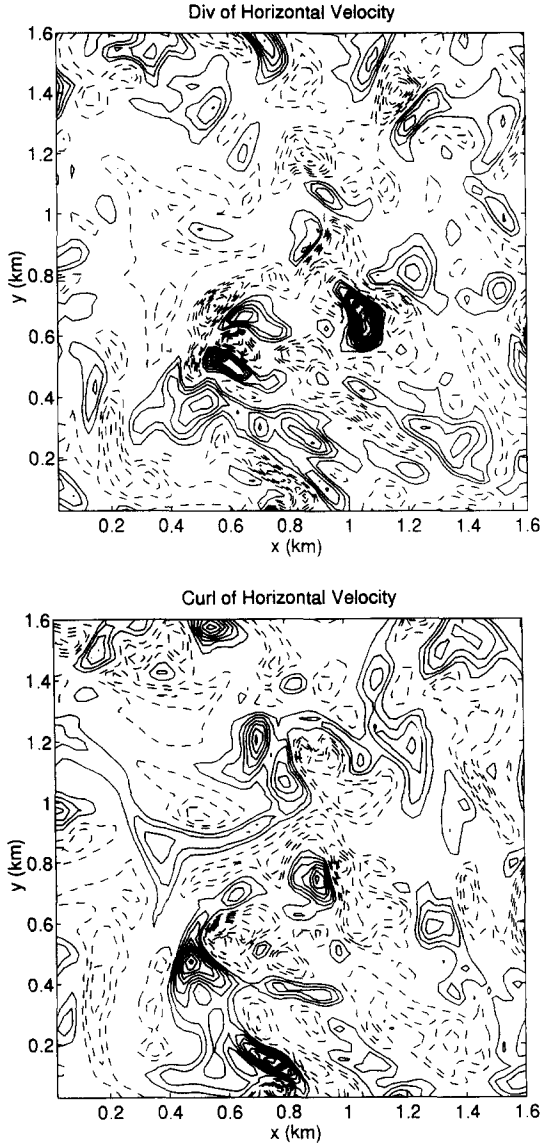


Fig. 3 (continued).

variance, whereas the three-dimensional runs all had strengths of less than 50%. For fixed Ro^* , the strength of the first mode increased monotonically as Ra_H decreased, and was most sensitive to Ra_H around $Ra_H \approx 10^6 - 10^8$ in the transition zone between the regimes.

4. Scaling of observed flow parameters

As described in the previous section, we observed two qualitatively different limits, a quasi-two-dimensional heton regime and a three-dimensional irregular regime. There does not appear to be a sharp transition from one limit to the other, but for the purposes of analysis, we divided the experiments into two groups, based on how quasi-two-dimensional the convection appeared to be. This judgment was supported and quantified by the EOF analysis described in Section 3.3. As shown in Fig. 1(a), the experiments to the left of the dotted line are designated the heton regime, and the experiments to the right are designated the three-dimensional regime. The laboratory experiments of FCB are, we believe, in the heton regime, as are the low Ro^* experiments of Boubnov and Golitsyn (1990) and Maxworthy and Narimousa (1994). We now consider the scaling appropriate to each regime separately, but for convenience display results for each in the same figure. We

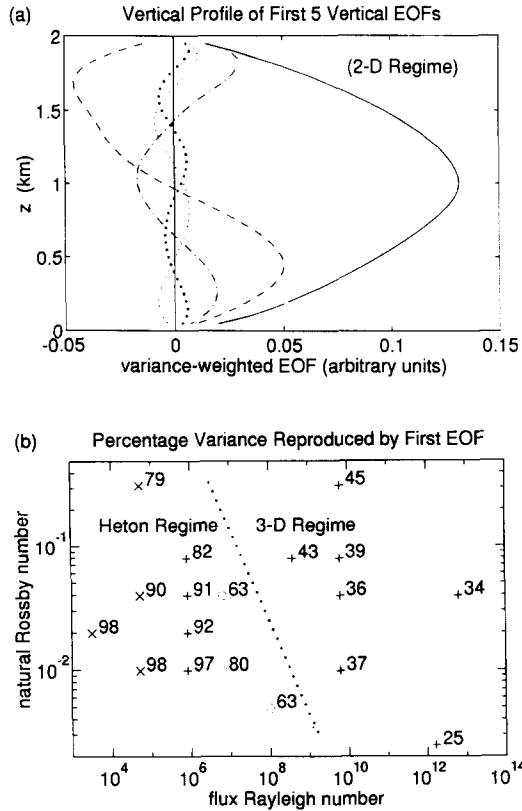


Fig. 4. (a) Vertical profiles of the five most significant empirical orthogonal functions of vertical velocity, weighted by variance associated with each EOF (Run 9, $Ro^* = 0.04$, $Ra_H = 6.4 \times 10^6$). (b) Percentage of variance of $w(x, y, z)$ reproduced by lowest-mode EOF as function of natural Rossby number and flux Rayleigh number. Dotted line shows approximate division between heton and three-dimensional regimes.

attempt to understand, to the extent that it is possible, the observed scales in terms of variations of the parameter Ro^* alone; we find that the flow characteristics are sensitive to moderate variations in Ro^* and, for the parameter range encompassed here, are much less sensitive to Ra_f . The key quantities describing the observed flow are mean stratification (this is the (adverse) stratification set up by the convection itself—the ocean was homogeneous in density before the onset of convection), horizontal eddy length scale, and the standard deviation of velocity and buoyancy. All the statistics evolved over time to a final stage in which there was little sign of any trend in the statistics. The time to reach the quasi-steady state was on the order of several rotation periods, and tended to increase with total fluid depth, rotation rate, and horizontal diffusivity. This time scale was also different for different statistics, with horizontal speed generally taking the most time to reach its approximate final value. The statistics were estimated from the time average of the final state; time variations in each statistic were such that the estimate of the time average was good to within about 5%.

4.1. The heton regime

4.1.1. Stratification

Although the whole domain was continuously losing heat as a result of cooling at the surface, the shape of the vertical profile of the horizontally averaged temperature at each vertical level attained an approximately steady state after cold water reached the bottom. The surface heat loss maintained a statically unstable temperature gradient for the duration of each run. In all runs, the stratification was characterized by a large buoyancy gradient near the surface and a somewhat smaller gradient over most of the water column (see Fig. 5(a), in which the profiles are normalized to emphasize the shape rather than the magnitude of the buoyancy profile). This is in agreement with the laboratory observations of Boubnov and Golitsyn (1990).

How might we expect the top-to-bottom buoyancy difference Δb to depend on B , H , and f ? Let us suppose that the buoyancy loss B at the surface is distributed over a depth h in time t . Then

$$\Delta b \approx Bt/h \quad (12)$$

If $t = h/w$ is the time it takes for a fluid particle to fall a distance h , where w is a typical downwelling speed, and if (see below) w scales with $U_{\text{rot}} = (B/f)^{1/2}$ then this time scale is h/U_{rot} (Send and Marshall (1994) called h/U_{rot} , t_{mix} , a time scale to mix properties over a depth h) implying that

$$\Delta b \approx (Bf)^{1/2} = G_{\text{rot}} \quad (13)$$

or equivalently, $\Delta b/G_{\text{non}} \approx Ro^{*-1/3}$. Another quantification of the adverse temperature gradient is to define an N^2 appropriate to statically unstable stratification:

$$N^2 = \frac{db}{dz} = g\alpha \left| \frac{dT}{dz} \right| \quad (14)$$

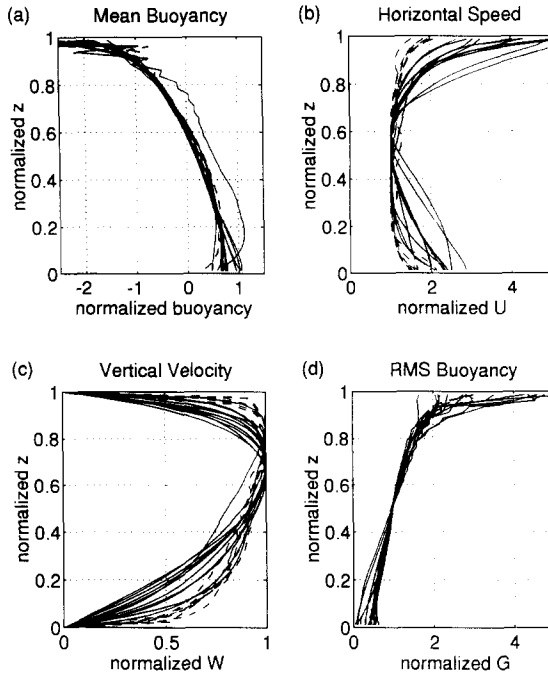


Fig. 5. Time-average vertical profiles of statistics—runs in two-dimensional regime denoted by continuous lines, in three-dimensional regime by dashed lines. Each vertical profile is normalized to emphasize the shape rather than the magnitude of the profile. (a) Mean buoyancy. (b) Mean horizontal speed U . (c) Standard deviation W of vertical component of velocity. (d) Standard deviation G of buoyancy.

It should be noted that (13) implies $N/f \propto Ro^{*1/2}$. For all runs, N was calculated from the average of $|dT/dz|$ over the middle half of the water column, where it is approximately constant. N/f tends to increase with Ro^* (Fig. 6(a)) and decrease with increasing Ra_f . A least-squares fit to all the experiments that fall in the heton regime yielded

$$N/f = 2.8Ro^{*1/3}Ra_f^{-1/12} \tag{15}$$

(In these and the succeeding presentations of results, we round the denominators of all exponents of (Ro^*, Ra_f) to the nearest integer.) The dependence shown in (15) is not far from the $Ro^{*1/2}$ dependence implied by (13), which is represented by the straight line in Fig. 6(a). Eq. (15) shows a dependence on the natural Rossby number that is in accord with Boubnov and Golitsyn’s (1990) results, which may be written

$$N/f = 1.5Ro^{*1/3}Ra_f^{-1/24} \tag{16}$$

when the parameters (Ta, Ra_f, Pr) are converted to (Ro^*, Ra_f, Pr) . Our numerical results also show weak dependence on Ra_f as in the laboratory findings. Values of N/f from the numerical runs, after normalizing with (15), are plotted in

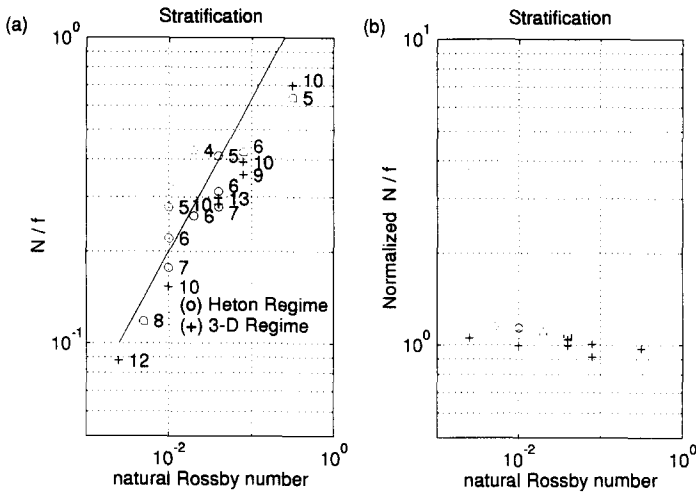


Fig. 6. Observed N/f as a function of natural Rossby number Ro^* for runs in the two-dimensional regime (o) and the three-dimensional regime (+). (a) Raw data, computed as described in text, with predicted curve $N/f = cRo^{*1/2}$ ($c = 2$). (b) Data normalized by least-squares fits, using Eq. (15) for the two-dimensional regime and Eq. (24) for the three-dimensional regime. In (a), numbers next to data points show common logarithms of Ra_f .

Fig. 6(b). It is also encouraging that the constant of proportionality in (15) and (16), 2.8 and 1.5 respectively, are of a similar magnitude.

4.1.2. Horizontal length scale

Length scales were computed from the autocorrelation function as a function of depth. The autocorrelations of the vertical velocity had a central peak surrounded by structures of smaller amplitude. The horizontal length scale of a field was defined to be the full width at half maximum (FWHM) of the central peak. The horizontal length scale measured in this way was roughly equivalent to one's subjective impression of eddy radius observed in contour plots of the flow fields as in Fig. 2, for example; they were on the order of hundreds of meters. The resulting numerical data is fitted well by the relation

$$L_w/H = 2.1Ro^{*1/4}Ra_f^{-1/10} \tag{17}$$

(see Fig. 7). This expression is close to the laboratory results of Boubnov and Golitsyn (1986), whose measurements are equivalent to

$$L/H = 3.6Ro^{*1/3}Ra_f^{-1/12}Pr^{1/3} \tag{18}$$

where their L is half the distance between neighboring eddy centers, and should be similar to our measure of eddy radius. Eq. (17) is even closer to the expression for horizontal length scale given by linear analysis (Nakagawa and Frenzen, 1955; Chandrasekhar, 1961), which in terms of our parameters is $L/H \propto Ro^{*2/9}Ra_f^{-1/9}Pr^{1/9}$. This suggests that linear theory gives a fairly good estimate of

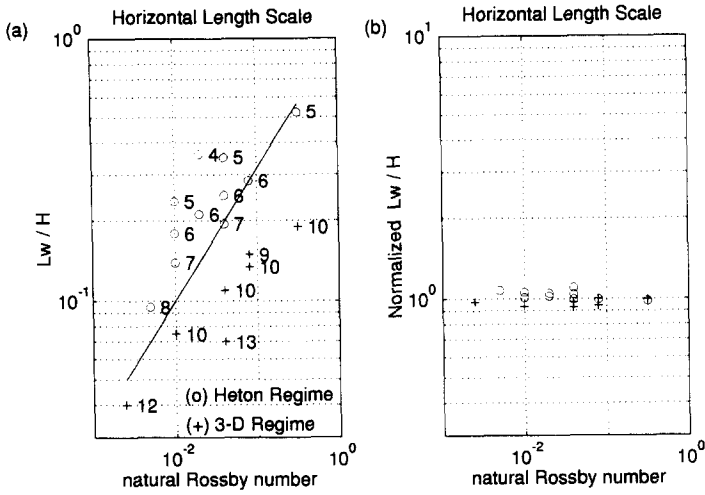


Fig. 7. Same as Fig. 6 but for quantity L_w/H . (a) Raw data, with predicted curve $L_w/H = Ro^{-1/2}$. (b) Data normalized using Eqs. (17) and (25). In (a), numbers next to data points show common logarithms of corresponding values of Ra_f .

L/H even for Ra_f orders of magnitude greater than its critical value for instability.

The length scale and stratification can be combined to form another nondimensional parameter, NH/fL , which may shed some light on the values of flow quantities observed in the convection experiments. Fig. 8 shows that in the heton regime NH/fL is close to unity. More precisely, we find

$$NH/fL = 1.26 \pm 0.10 \tag{19}$$

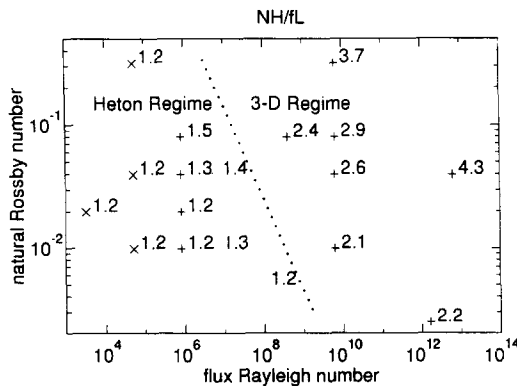


Fig. 8. Numbers show NH/fL as a function of flux Rayleigh number Ra_f and natural Rossby number Ro^* . As in Fig. 1, symbol type denotes ratio of horizontal to vertical diffusivity γ .

Combination of the expressions N/f and L_w/H (Eqs. (15) and (17)) actually yields a factor of $Ro^{*1/12} Ra_f^{1/60}$, which are such weak dependences that we cannot detect them. If $N/f \propto Ro^{*1/2}$ as suggested by the physical argument leading to (13), and $NH/fL \approx 1$, then the implied variation of L_w/H is $Ro^{*1/2}$ also. As seen in Fig. 8(a), there is much scatter but the points do cluster around a line with a slope of one-half. For each set of experiments with constant Ra_f , however, the points lie on a line of somewhat shallower slope which is better fitted by the $Ro^{*1/4}$ dependence of Eq. (17).

It is of significance and interest that the (adverse) stratification and horizontal scale should adjust so that NH/fL is unity. The scale NH/f is the long-wave cut-off of the Chandrasekhar (1953) stability problem (see also Davey and Whitehead (1981)). Linear waves which have a scale greater than this pseudo-Rossby radius are stabilized by rotation. It represents the scale at which the overturning forces associated with the adverse temperature gradient measured by N are balanced by the counter-overturning forces associated with rotation. It is on this scale that these two effects are in balance and that we observe our convective elements.

4.1.3. Speeds

At each level, we measured the standard deviation of b and w as well as the quantity $U = (\langle u^2 + v^2 \rangle)^{1/2}$ ($\langle \rangle$ indicates the horizontal average over the domain of integration). Owing to the influence of rigid boundaries, W , the standard deviation of vertical velocity, had a broad maximum in the center of the water column (Fig. 5(c)) whereas the tendency of circulations to form near the upper and lower surfaces caused horizontal speed standard deviations to have maxima at the top and bottom of the domain (Fig. 5(b)).

Each statistic was averaged in time over the quasi-steady stage of the run and in space over the lower half of the domain. Both U and the W were found to be proportional to U_{rot} , as reported by Boubnov and Golitsyn (1990), FCB and Jones and Marshall (1993), but a weak dependence on the flux Rayleigh number was also found. Least-squares fit to the data yielded

$$U/U_{rot} = 0.25 Ra_f^{1/10} \quad (20)$$

and

$$W/U_{rot} = 0.14 Ra_f^{1/8} \quad (21)$$

Plots of U before and after normalization by Eq. (20) are shown in Fig. 9. It should be noted that these data were much noisier than the statistics for N and L_w . Normalizing N/f and L_w/H with the scalings given above reduced the standard deviation of these statistics (based on the 11 data points from 11 runs) from 36% and 47%, respectively, to about 3% in each case, whereas normalizing the speed statistics, which had similar standard deviation of about 40% before normalization, only reduced the standard deviation to around 15% of the mean.

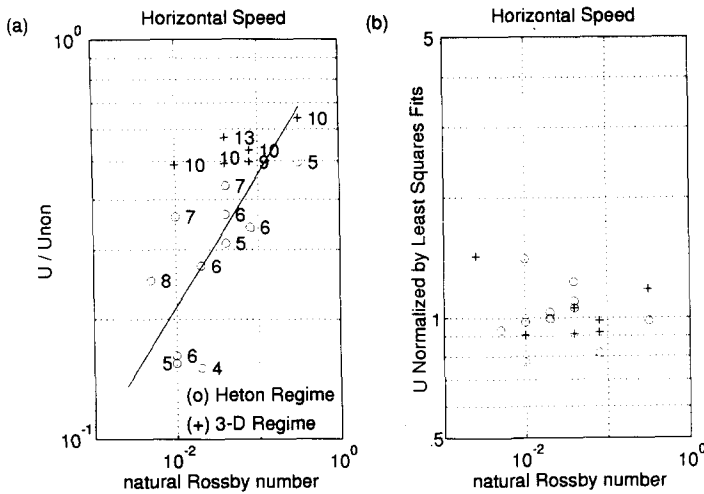


Fig. 9. Same as Fig. 7 but for horizontal speed U . (a) Raw data. (b) Data normalized using expressions in Eqs. (20) and (26). In (a), numbers next to data points show common logarithms of Ra_f .

4.1.4. Rossby and hydrostatic numbers

The Rossby number $Ro = U/fL$ of the flow (see Fig. 1(b)) was computed using L_w as the measure of the horizontal length scale and U as defined above. Ro increased with increasing natural Rossby number, as one would expect, and also increased with Ra_f , because as friction is decreased, smaller, faster structures can appear, thus raising the value of Ro .

A more direct measurement of geostrophy was made in selected runs. The geostrophic velocity $(u_g, v_g) = (-\partial p/\partial y, \partial p/\partial x)/(f\rho_0)$ was calculated from the pressure field at several levels in the water column. The ageostrophic velocity, defined as the difference between the actual velocity and the geostrophic velocity, was also computed and compared with the geostrophic velocity by taking the ratio of the variances of ageostrophic and geostrophic speeds u_a/u_g . For $Ro \leq 0.9$, $u_a/u_g \approx 2Ro$, and for $Ro > 0.5$, $u_a/u_g \approx 1$. Thus for ageostrophic velocities to be smaller than geostrophic velocities, we must have $Ro < 0.5$.

It is also of interest to ascertain to what extent the convective structures modeled here are in hydrostatic balance. As pointed out by Brugge et al. (1991), a flow characterized by speed, length, and buoyancy frequency scales U , L , and N will be hydrostatic when $(U/LN)^2 \ll 1$. As shown in Fig. 10, $(U/LN)^2$ decreases with both decreasing Ro^* and Ra_f . The hetons had rather small values of this hydrostatic parameter ($(U/LN)^2$ varied from 0.01 to 0.85), and as they also had small Ro , they are in thermal wind balance.

4.1.5. Buoyancy

Vertical profiles of G , the standard deviation of buoyancy, had broadly the same shape for all the experiments, with greatest values at the top of the water column (see Fig. 5(d)). Hydrostatic and geostrophic flow obeys the thermal wind

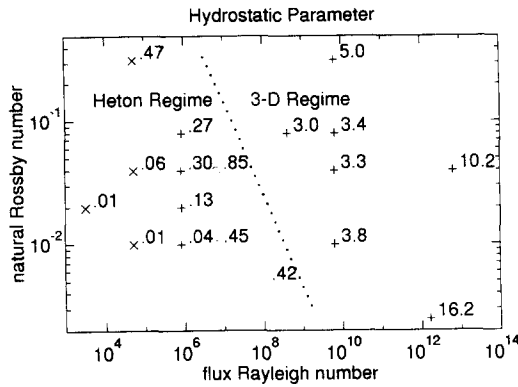


Fig. 10. Numbers show hydrostatic parameter $(U/LN)^2$ as a function of Ra_f and Ro^* . Symbol types as in Fig. 1.

relation, which implies that $fUL/GH \approx 1$. This implies that $G \approx fUL/H$, which for the observed scalings of L_w/H and U (Eqs. (17) and (20)) recorded above implies that $G \approx G_{non}Ro^{*1/12}$ and so is essentially independent of rotation; we can neglect one-twelfth power dependence on Ro^* , which is in the noise level of our experiments. The actual buoyancy standard deviation in the heton regime was observed to be

$$G = (1.0 \pm 0.25)G_{non} \tag{22}$$

The somewhat large scatter in the coefficient did not show any significant trend (see Fig. 11). The observed scalings of U , L_w/H and G then combine to give us

$$fUL/GH = 0.78 \pm 0.16 \tag{23}$$

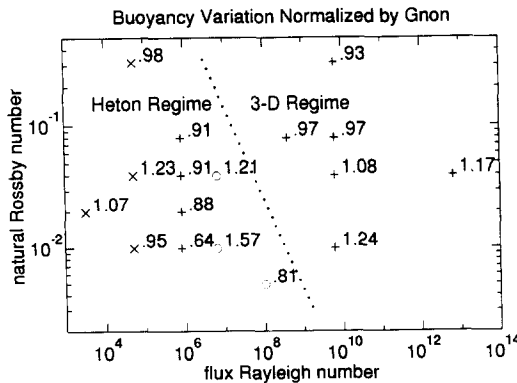


Fig. 11. Normalized buoyancy variance G/G_{non} as a function of Ra_f and Ro^* . Symbol types as in Fig. 1.

The result (22) for G differs from both that of FCB and Boubnov and Golitsyn (1990), who found that G scaled with G_{rot} , but is dynamically self consistent. In other words, to the extent that the convective structures are under geostrophic and hydrostatic control, (22) is the only consistent scaling for G , given (17) and (20). Using Boubnov and Golitsyn's scalings for L/H , U , and G would imply $fUL/GH \approx \text{Ro}^{*1/3} \text{Ra}_f^{-1/12}$ and so violate either geostrophy or the hydrostatic assumption. The discrepancy can perhaps be explained by high-mode vertical structures which may have existed in some of Boubnov and Golitsyn's runs and which were observed by FCB. When the motion is three-dimensional, the appropriate vertical length scale for the thermal wind can no longer be assumed to be H .

4.1.6. Effect of anisotropic diffusivity

One factor that complicates the comparison of numerical experiments with the laboratory experiments is the use of an anisotropic diffusivity of heat and momentum in some of our runs in the two-dimensional regime. To investigate whether such a procedure produces results which differ from those employing an isotropic diffusivity, a simulation with high horizontal and low vertical diffusivity ($(\kappa_H, \kappa_V) = (1, 0.1) \text{ m}^2 \text{ s}^{-1}$) was repeated with all parameters the same except for the vertical diffusivity, which was raised to $1 \text{ m}^2 \text{ s}^{-1}$ (see Runs 9 and 8 in Table 2(a)). A comparison of the two runs showed that the flow fields were qualitatively the same and the flow statistics were very similar. The vertical temperature gradient and the standard deviations of temperature, horizontal speed, and vertical speed of the high κ_H run differed by at most only 15% from the corresponding value in the low κ_H run. Similarly, L_w in the high κ_H run was within 5% of its value in the other run. This implies that a convecting fluid, at least in the parameter regime of our experiments, in which the diffusion terms are smaller than the inertial terms in the equations of motion, is insensitive to the precise value of the smaller of the (anisotropic) diffusivity components.

4.2. Three-dimensional regime

The three-dimensional regime was characterized by Ro of order unity and by nonhydrostatic effects (see Figs. 1(b) and 10). Thus, the thermal wind scalings are not appropriate and cannot be used to constrain the various scalings. Moreover, the vertical scale was not set by H as in the heton regime. The dependence of the flow quantities on external parameters was again measured.

A least-squares fit to the stratification parameter N/f (see Fig. 6) yields a dependence on Ro^* that is similar to that of the heton regime (Eq. (15)) and even closer than (15) to the $\text{Ro}^{*1/2}$ dependence derived using the physical arguments that led up to Eq. (13):

$$N/f = 1.2 \text{Ro}^{*4/9} \quad (24)$$

It should be noted that although N/f is more sensitive to Ro^* and hence to f than in the two-dimensional case, N is actually somewhat less strongly dependent on f ($N \propto f^{1/3}$ in the three-dimensional regime and $N \propto f^{1/2}$ in the heton

regime). This is consistent with the lesser degree of geostrophy exhibited in this regime. However, L_w/H had essentially the same dependence on Ro^* and Ra_f as observed in the field of hetons (see Fig. 7):

$$L_w/H = 1.0Ro^{*1/4}Ra_f^{-1/17} \quad (25)$$

Although both Eqs. (24) and (25) are similar to the corresponding expressions for the heton regime, in the three-dimensional regime NH/fL ranged between two and four, and tended to increase with Ro .

In contrast to N/f and L_w/H , the horizontal speed and vertical velocity had no significant dependence on Ro^* (see Fig. 9 for horizontal speed). Normalizing with the nonrotating velocity scale, we obtain

$$U/U_{\text{non}} = 0.54 \pm 0.06 \quad (26a)$$

$$W/U_{\text{non}} = 0.42 \pm 0.05 \quad (26b)$$

As in the heton regime, G also had negligible dependence on Ro^* (see Fig. 11):

$$G/G_{\text{non}} = 1.1 \pm 0.1 \quad (27)$$

The scalings exhibited by the three-dimensional regime in our experiments are indicative of an intermediate state between nonrotating convection and geostrophic convection. In this transition region, rotation seems to influence the horizontal scale of the convective elements as well as the mean stratification, but does not appear to influence the magnitude of the convective elements as measured by U , W , and G .

5. Conclusions

Numerical experiments with a high-resolution nonhydrostatic model of convection in a rotating, initially unstratified domain produced a field of eddies whose characteristics depended on the natural Rossby number $Ro^* = (B/f^3H^2)^{1/2}$ and the flux Rayleigh number $Ra_f = BH^4/\kappa^2\nu$ (the Prandtl number, or ratio of momentum diffusivity to heat diffusivity, was unity in all our experiments). We can think of Ro^* as a measure of the importance of rotation and Ra_f as a measure of the importance of diffusion of heat and momentum; increasing Ro^* and Ra_f decreases the effects of rotation and diffusion, respectively. In the parameter regime of our experiments, $0.0025 \leq Ro^* \leq 0.32$ and $3 \times 10^3 \leq Ra_f \leq 6 \times 10^{12}$, we confirmed that the characteristics of the flow were sensitive to moderate changes in Ro^* (factors of two) and large changes in Ra_f (factors of 1000).

In rotating convection, buoyancy forces which tend to mix the fluid vertically are opposed by the effects of diffusion (or small-scale turbulent mixing) and rotation. On the one hand, convection creates regions of horizontal divergence and convergence as light water rises and dense water sinks. Diffusion tends to suppress motion on small scales, so that in nonrotating systems, upwelling and downwelling

regions have a horizontal scale which is typically comparable with the depth of the unstable fluid, which in deep oceanic convection is a few kilometers. On the other hand, rotation causes flow on sufficiently large scales to approach geostrophic balance, which is nondivergent. This is consistent with the observation that the horizontal length scale decreases with increased rotation and increases with increased diffusion.

We presented physical arguments, which we briefly again draw together now, that predict the key scales observed (and which were broadly supported by our experiments). At sufficiently small Ro^* , the magnitude of the adverse buoyancy gradient Δb , maintained by rotation in the face of surface cooling, varies as $(Bf)^{1/2}$. This may be expressed equivalently in term of N , thus:

$$\frac{N}{f} \approx Ro^{*1/2} \quad (28)$$

(the straight line drawn in Fig. 7(a)). The horizontal length scale of the ensuing convection is such that

$$NH/fL \approx 1 \quad (29)$$

suggesting that

$$\frac{L}{H} \approx Ro^{*1/2} \quad (30)$$

(the straight line in Fig. 8(a)). Furthermore, if $U \approx U_{rot}$ as observed in the heton regime, then if the flow is in geostrophic and hydrostatic (and hence thermal wind) balance, we obtain

$$G \approx \frac{fUL}{H} \quad (31)$$

which, combined with (30) implies that G is independent of Ro^* .

The above scalings are broadly supported by our numerical experiments (in the quasi-two-dimensional regime); the points in Figs. 7(a), 8(a), and 10(a) do cluster around the straight lines plotted on the basis of the above simple considerations. Because our experiments were not (and indeed cannot be) carried out at sufficiently high Rayleigh number, the observed scales show a dependence on Ra_f also; they deviate somewhat from the scales predicted above and exhibit a more complicated dependence on both Ro^* and Ra_f . However, we find that this dependence was broadly in accord with that observed in laboratory experiments carried out in the same parameter regime. The relation $NH/fL \approx 1$, the long-wave cut-off of (linear) rotating Rayleigh theory, was found to hold in the heton regime, even though the flux Rayleigh number was high enough so that nonlinear effects were potentially important.

Rotation and diffusion both act to inhibit the vertical transport of buoyancy and so lead to a greater unstable density gradient. Our experiments do indeed exhibit

increasing vertical density gradient for decreasing Ro^* , and decreasing Ra_f : in the heton regime, $N/f = 2.4Ro^{*1/3}Ra_f^{-1/12}$, and in the three-dimensional regime, $N/f = 1.2Ro^{*1/2}$. This is similar to the dependence found by Boubnov and Golitsyn (1990), $N/f \propto Ro^{*1/3}Ra_f^{-1/24}$ in the laboratory. Chan (1974), whose results formally were limited to the case of infinite Prandtl number, arrived at such a scaling by maximizing the vertical heat flux produced by a given unstable stratification.

As described above, we would expect the effects of diffusion and rotation on eddy size to work in opposite senses, because diffusion suppresses motion at small scales, whereas geostrophy suppresses vertical motion on large scales. Accordingly, the horizontal length scale of the convective motion was best fitted by the expression $L_w/H = 2.1Ro^{*1/4}Ra_f^{-1/10}$ for runs in the heton regime and by $L_w/H = 1.0Ro^{*1/4}Ra_f^{-1/17}$ in the three-dimensional regime. Both scalings are close to the laboratory observations of Boubnov and Golitsyn (1986).

The behavior of the horizontal and vertical speed scales were different in the heton and three-dimensional regimes. In the heton regime, U and W were both proportional to $U_{rot} = (B/f)^{1/2}$, but in the three-dimensional regime, U and W were closer to the nonrotating velocity scale $U_{non} = (BH)^{1/3}$. In both regimes, G , the horizontal variation in buoyancy, was virtually independent of f .

It is likely that the more complicated structure of the flow in the three-dimensional regime is due to an instability of the lowest-vertical-mode convection cells. If that instability were inhibited by viscosity, then one would expect that the vertical structure might be a function of the Reynolds number, $Re = UL/f$. If we use the observed heton regime scaling for U and L (ignoring the weak dependences on Ra_f) and express ν in terms of Ra_f , we find that the approximate dependence is $Re \approx (Ro^{*2}Ra_f)^{1/3}$. This implies that the transition from the heton limit to the three-dimensional limit should occur in a direction normal to the curves in which $Ro^* \approx Ra_f^{-1/2}$. This indeed is observed: the dotted line in Fig. 1(a) has a slope of approximately $-\frac{1}{2}$, strengthening the hypothesis that the Reynolds number is the important parameter governing the transition.

It is difficult to apply numerical and laboratory results directly to the ocean, largely because of the sparsity and nature of the observations at the relevant time and space scales. However, deep convection in the ocean appears to be in a regime in which $Ro^* \leq 1$. Evidence from the MEDOC experiments suggests that $Ro^* \approx 0.3$ in deep-reaching convection, and so rotation may have an influence on the convective elements. The explicit diffusivity employed in our simulations is best thought of as a simple parameterization of unresolved convective scales—an eddy diffusivity. The appropriate diffusivity for a convecting chimney in the ocean is poorly known. One practical way forward might be to infer Ra_f from available observations. For example, in the recent observations of Schott and Leaman (1991) in the Gulf of Lions, one observes horizontal currents of approximately 5 cm s^{-1} in a chimney of 2 km in depth, forced by cooling at rates of about 500 W m^{-2} , giving $Ro^* \approx 0.24$. If the ocean was in the heton regime, $U_{rot} \approx 4 \text{ cm s}^{-1}$, and so if our scaling is appropriate, $Ra_f \approx 10^7$ and $\kappa \approx 0.6 \text{ m}^2 \text{ s}^{-1}$. For $H \approx 2 \text{ km}$ this predicts $L \approx 500 \text{ m}$, which is broadly consistent with observations.

Acknowledgments

B.A.K. conducted this research under the NOAA Atlantic Climate Change Program. J.M. was supported in part by the Office of Naval Research. Tom Yates and Christopher Hill provided computer assistance (Tom Yates was funded, in part, by an EEC MERMAIDS MAST grant).

References

- Boubnov, B.M. and Golitsyn, G.S., 1986. Experimental study of convective structures in rotating fluids. *J. Fluid Mech.*, 167: 503–531.
- Boubnov, B.M. and Golitsyn, G.S., 1988. Thermal structure and heat transfer of convection in a rotating fluid layer. *Dokl. Akad. Nauk SSSR*, 300: 350–353.
- Boubnov, B.M. and Golitsyn, G.S., 1990. Temperature and velocity field regimes of convective motions in a rotating plane fluid layer. *J. Fluid Mech.*, 219: 215–239.
- Boubnov, B.M. and Ivanov, V.N., 1988. Time dependent spectrum of temperature fluctuations for free turbulent convection in a fluid layer. *Izv. Atmos. Ocean Phys.*, 24: 361–367.
- Brickman, D. and Kelley, D.E., 1994a. Development of convection in a rotating fluid: scales and patterns of motion. *Dyn. Atmos. Oceans*, 19: 389–405.
- Brickman, D. and Kelley, D.E., 1994b. Rotating convection: scales and regimes. *Dyn. Atmos. Oceans*, submitted.
- Brugge, R., Jones, H.L. and Marshall, J.C., 1991. Non-hydrostatic ocean modelling for studies of open-ocean deep convection. In: P.C. Chu and J.C. Gascard (Editors), *Deep Convection and Deep Water Formation in the Oceans*. Elsevier, Amsterdam, pp. 325–340.
- Chan, S.K., 1974. Investigation of turbulent convection under a rotation constraint. *J. Fluid Mech.*, 64: 477–506.
- Chandrasekhar, S., 1953. The instability of a layer of fluid heated below and subject to Coriolis forces. *Proc. R. Soc. London, Ser. A*, 217: 306–327.
- Chandrasekhar, S., 1961. *Hydrodynamic and Hydromagnetic Stability*. Dover, New York.
- Chen, R., Fernando, H.J.S. and Boyer, D.L., 1989. Formation of isolated vortices in a rotating convecting fluid. *J. Geophys. Res.*, 94: 18445–18453.
- Davey, M.K. and Whitehead, J.A., 1981. Rotating Rayleigh–Taylor instability as a model of sinking events in the ocean. *Geophys. Astrophys. Fluid Dyn.*, 17: 2219–2231.
- Fernando, H.J.S., Boyer, D.L. and Chen, R., 1989. Turbulent thermal convection in rotating stratified fluids. *Dyn. Atmos. Oceans*, 13: 95–121.
- Fernando, H.J.S., Chen, R. and Boyer, D.L., 1991. Effects of rotation on convective turbulence. *J. Fluid Mech.*, 228: 513–547.
- Golitsyn, G.S., 1980. Geostrophic convection. *Dokl. Akad. Nauk SSSR*, 251: 1356–1360.
- Harlow, R.H. and Welch, J.E., 1965. Time dependent viscous flow. *Phys. Fluids*, 8: 2182–2193.
- Hogg, N. and Stommel, H., 1985. The heton, an elementary interaction between discrete baroclinic vortices, and its implication concerning eddy heat-flow. *Proc. R. Soc. London, Ser. A*, 397: 1–20.
- Jones, H. and Marshall, J., 1993. Convection with rotation in a neutral ocean; a study of open-ocean deep convection. *J. Phys. Oceanogr.*, 23: 1009–1039.
- Leaman, K.D. and Schott, F., 1991. Hydrographic structure of the convection regime in the Gulf of Lions: Winter 1987. *J. Phys. Oceanogr.*, 21: 573–596.
- Legg, S. and Marshall, J., 1993. A heton model of the spreading phase of open-ocean deep convection. *J. Phys. Oceanogr.*, 23: 1040–1056.
- Mason, P.J., 1989. Large-eddy simulation of the convective atmospheric boundary layer. *J. Atmos. Sci.*, 46: 1492–1515.
- Maxworthy, T. and Narimousa, S., 1991. Vortex generation by convection in a rotating fluid. *Ocean Modelling*, 92: 1037–1040.

- Maxworthy, T. and Narimousa, S., 1994. Unsteady, turbulent convection into a homogeneous, rotating fluid. *J. Phys. Oceanogr.*, 24: 865–887.
- Nakagawa, Y. and Frenzen, P., 1955. A theoretical and experimental study of cellular convection in rotating fluid. *Tellus*, 7: 1–21.
- Raasch, S. and Etling, D., 1991. Numerical simulation of rotating turbulent thermal convection. *Contrib. Atmos. Phys.*, 3: 1–15.
- Schott, F. and Leaman, K.D., 1991. Observations with moored acoustic Doppler current profilers in the convection regime in the Gulf of Lions. *J. Phys. Oceanogr.*, 21: 556–572.
- Send, U. and Marshall, J., 1994. Integral effects of deep convection. *J. Phys. Oceanogr.*, 24: 000–000.
- Veronis, G., 1958. Cellular convection with finite-amplitude in a rotating fluid. *J. Fluid Mech.*, 5: 410–435.